 doi:10.20944/preprints202210.0389.v1

Article

Photon-phonon atomic coherence interaction of non-linear signals in various phase transitions Eu^{3+}: $BiPO_4$

Huanrong Fan#, Faizan Raza#, Irfan Ahmed, Muhammad Imran, Faisal Nadeem, Changbiao Li*, Peng Li*, and Yanpeng Zhang*

Key Laboratory for Physical Electronics and Devices of the Ministry of Education & Shaanxi Key Lab of information Photonic Technique, Xi'an Jiaotong University, Xi'an 710049, China; 495356182@qq.com (H.F.); faizanraza17@outlook.com (F.R.); irfan.ahmed@my.cityu.edu.hk (I.A.); imran89@mail.xjtu.edu.cn (M.I.); faisalnadeem15@stu.xjtu.edu.cn (F.N.); cbli@mail.xjtu.edu.cn (C. L.); ponylee@stu.xjtu.edu.cn (P.L.); ypzhang@mail.xjtu.edu.cn (Y.Z.)

* Correspondence: ypzhang@mail.xjtu.edu.cn, ponylee@stu.xjtu.edu.cn, cbli@mail.xjtu.edu.cn

\# These authors contributed equally to this work.

Abstract: We report photon-phonon atomic coherence (cascade- and nested-dressing) interaction from various phase transitions of Eu^{3+}: $BiPO_4$ crystal. Such atomic coherence spectral interaction evolves from out of phase fluorescence to in-phase spontaneous four-wave mixing (SFWM) by changing the time gate. The dressing dip switch and three dressing dips of SFWM result from strong photon-phonon destructive cross- and self-interaction for hexagonal phase, respectively. The more phonon dressing result in destructive interaction, while less phonon dressing result in constructive interaction of atomic coherences. The experimental measurements of photon-phonon interaction agree with theoretical simulations. Based on our results, we proposed a model for an optical transistor (as an amplifier and switch).

Keywords: atomic coherence, spectral interaction, phonon/photon dressing; spontaneous four-wave mixing

1. Introduction

In the past years, it was desirable to couple a single like-atom spin to a superconducting qubit, where a nanomechanical resonator is coupled to a two-level system to induce strong phonon-phonon interactions [1-2]. However, the entanglement generated is affected by different systems in a traditional method that often needs a strong spin-phonon interaction to exceed the decay of the phonons [3-4]. Phonon dispersion relation and lattice-spin coupling of Eu3+ have been reported [5-6]. Thermal phonon at elevated temperatures, lattice vibration structural transition, and thermal expansion behavior in $LaPO_4$: Eu have been also studied [7].

Recently, the photon-phonon dressing coupling in Eu^{3+} ions doped $BiPO_4$ has been studied [8-9], as Eu^{3+}/ Pr^{3+} ions are very sensitive to the site symmetry and its surrounding crystal field of the host material than other crystal ions [10-12]. Therefore, it can be achievable to get such kind of potential application in $BiPO_4$ crystal. The crystal structure of $BiPO_4$ has two polymorphic forms, monoclinic (M)- and hexagonal (H)-phases. The difference in the symmetry of the lattice structure results in different interactions [13-14]. The H-phase of crystal is more structurally asymmetric than the M-phase in Eu^{3+} because of a more atomic-like system. Bismuth phosphate ($BiPO_4$) has drawn significant attention as a host medium for doping lanthanide ions due to its comparable ionic radius of Bi^{3+}(1.11 Å) with that of lanthanide ions [15-17].

Preprints (www.preprints.org) | NOT PEER-REVIEWED | Posted: 25 October 2022 doi:10.20944/preprints202210.0389.v1

The Eu^{3+}: $BiPO_4$ is one of the most promising atomic-like mediums known for its long coherence time (ms) [8] due to photon-phonon coupling in doubly dressed states with potential applications in quantum memory [18-20].

Interactions of doubly dressed states and the corresponding properties of atomic systems have attracted considerable attention in recent decades. In this regard, two kinds of doubly dressed processes (in cascade- and nested-parallel schemes) were reported in an open five-level atomic system [21-22]. Nie et al theoretically investigated the similarities and differences between different kinds of singly dressing schemes for six-wave mixing to examine the interaction between multi-wave mixing in a five levels atomic system [23].

Next, we will consider such multi-nonlinear signals interaction with the coupling of lattice vibration phonon and photon dressing.

In this paper, we investigated two multi-dressing cross-interaction obtained from various phase transitions of Eu^{3+}: $BiPO_4$ crystal by changing time gates. The spectral cross-interaction evolves from out of phase FL, to hybrid (FL+SFWM), and to in-phase SFWM (anti-Stokes signal). Moreover, we demonstrate that the FL and SFWM destructive interaction results from more phonon dressing, and such dressing is achieved with multiparameter temperature (300K), H-phase, and broadband excitation.

2. Experimental Scheme

The ion PO_4^{3-}: [Bi^{3+}+Eu^{3+}] has five molar ratios (7:1, 20:1, 6:1, 1:1, 0.5:1) for Eu^{3+}: $BiPO_4$ sample with different lattice vibration structures. In our experiment (Fig.1(c)), we used five $BiPO_4$ samples with different combinations and concentrations of pure H-phase and low-temperature monoclinic phase (LTMP), where H-phase refers to C_2, and LTMP refers to C_1 site symmetry, respectively. The sample (7:1) corresponds to the pure M-phase, (20:1) corresponds to the mixed [more M (75%) + less H (25%)] phase, (6:1) corresponds to the mixed [half H (50%) + half M (50%)] phase, (1:1) corresponds to the mixed [less H (25%) + more M (75%)] phase, and (0.5:1) corresponds to the pure-H phase. The concentration of Eu^{3+} ions is 5% consistent across all five samples with different phase transitions. Figure 1(a) shows the fine structure energy levels of Eu^{3+}: $BiPO_4$ crystals. The Eu^{3+}: $BiPO_4$ has ground state $^7F_1$ and excited state $^5D_0$ (mj=0), the ground state 7F1 can split into mj=-1 (587.3nm), mj=0 (592.3nm), and mj=+1 (597.3nm) under the crystal field effect of BiPO4 crystal.

To implement the experiment, Eu3+: BiPO4 samples were held in a cryostat (CFM-102). The temperature was controlled through liquid nitrogen from 300K (large phonon Rabi frequency G_{pi}^{T} with more thermal phonons) to 77K, where $G_{pi}^{T} = -\mu_{kl} E_{pi} / \hbar$ is the Rabi frequency of phonon field (i=1, 2; T= (T1, T2) = (300K, 77K)). The μ_{kl} is the dipole moment between $|k\rangle$and $|l\rangle$ of crystal field splitting in $^7F_1$ state (Fig. 1(b)), E_{pi} is the phonon field, where such phonon builds atomic coherence for crystal field splitting in $^7F_1$.

In the experiment, the G_{pi}^{T} and phase transition detuning Δ_{pi}^{j} are controlled by temperature and different samples, respectively. The frequency detuning of phonon field is $\Delta_{pi}^{j} = \Omega_{kl} - \omega_{pi}^{j}$ (j=a(7:1), b(20:1), c(6:1), d(1:1) and e(0.5:1) sample) in Figure. 1(b), where Ω_{kl} is the frequency between $|k\rangle$ and $|l\rangle$. The ω_{pi}^{j} is the phonon frequency of the phonon field, which is determined by the vibration frequency of crystal lattice state mode. The different frequencies of phase transitions ($\omega_{pi}^{a} < \omega_{pi}^{e}$, $\Delta_{pi}^{a} > \Delta_{pi}^{e}$) can couple to different lattice vibrations for Eu^{3+}: $BiPO_4$, resulting in different phonon dressing ($|G_{pi}^{T}|^2 / i\Delta_{pi}^{a} < |G_{pi}^{T}|^2 / i\Delta_{pi}^{e}$).

Figure 1(c) shows the schematic diagram of the experimental setup. Here we used two tunable dye lasers (narrow scan with a 0.04cm^{-1} linewidth) pumped by an injection-locked single-mode Nd^{3+}: YAG laser (Continuum Powerlite DLS 9010, 10Hz repetition

Preprints (www.preprints.org) | NOT PEER-REVIEWED | Posted: 25 October 2022 doi:10.20944/preprints202210.0389.v1

rate, 5ns pulse width) to generate the pumping fields broadband E_1 (ω_1, Δ_1) and narrowband E_2 (ω_2, Δ_2). Broadband excitation E_1 couples to more crystal field splitting levels $^5D_0$ and $^7F_1$ (Fig. 1(b)), resulting in more lattice vibration (phonon dressing). However, narrowband excitation E_2 couples to fewer splitting levels, resulting in less lattice vibration. The frequency detuning here is $\Delta_i = \Omega_{mn} - \omega_i$, where Ω_{mn} is the frequency between crystal field splitting levels $^5D_0$ and $^7F_1$, ω_i is the optical frequency. The Rabi frequency of the optical field is defined as $G_i = -\mu_{mn} E_i / \hbar$, where μ_{mn} is the dipole moment of the crystal field splitting with different states $^5D_0$ and $^7F_1$ excited by E_i between levels $|m\rangle$ and $|n\rangle$ in Fig. 1(b). Such photon builds atomic coherence of crystal field splitting with different states ($^5D_0$ and $^7F_1$). The pulse generated from Nd^{3+}: YAG laser is used to simultaneously trigger a boxcar gated integrator and oscilloscope. The input laser beams are along the [010] axis of the $BiPO_4$ crystal, which is perpendicular to the optical axis. The spectral optical outputs are obtained by scanning laser frequency. The grating motor of two dye lasers is scanned by a computer to form the x-axis, and the intensity of the excitation spectrum is the average of ten shots from the gated integrator (Fig. 1(c)) appearing on the y-axis.

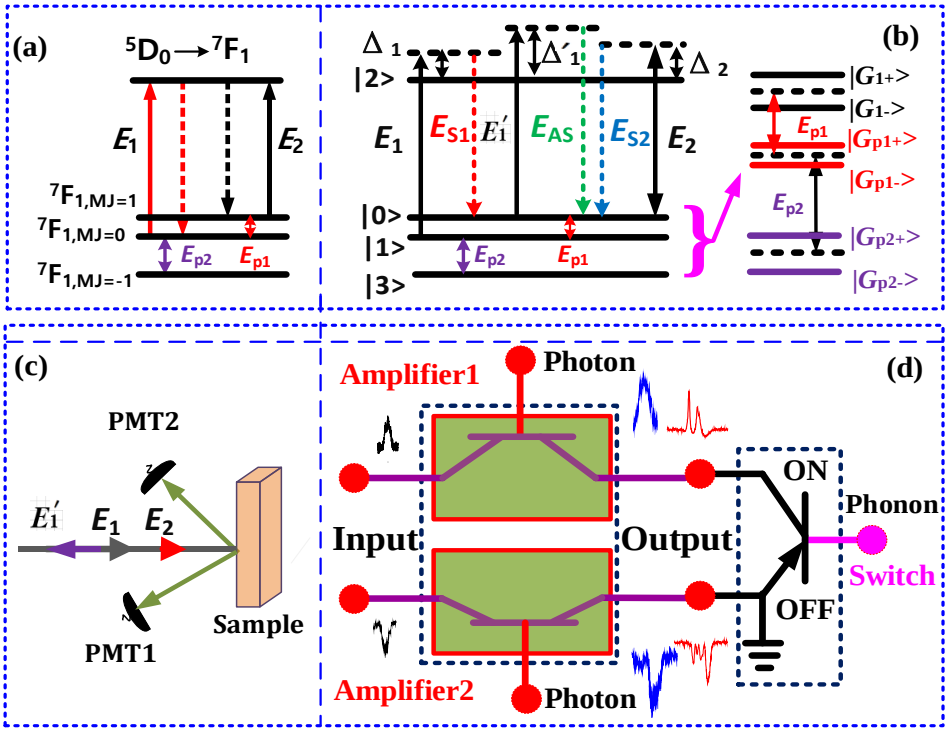

Fig. 1 (a) Show energy levels of Eu^{3+}: $BiPO_4$ for transition $^7F_1 \rightarrow {}^5D_0$, (b) Show photon and phonon four dressing energy level. (c) Experimental setup. (d) The schematic diagram of proposed optical transistor as an amplifier and switch.

The optical signal generated from Eu^{3+}: $BiPO_4$ crystal is detected via confocal lenses at photomultiplier tubes (PMTs). In our experiment setup, PMT1 is precisely placed to detect the narrowband FL and spontaneous four-wave mixing (SFWM) signal whereas PMT2 is placed to detect the broadband FL and SFWM signal. Such detector placement is

Preprints (www.preprints.org) | NOT PEER-REVIEWED | Posted: 25 October 2022 doi:10.20944/preprints202210.0389.v1

based on the different distances from the detector to the sample (Fig. 1(c)). Hence, PMT affects the ratio of out of phase FL and in-phase SFWM. The out of phase FL1 signal and FL2 signals are generated through excitation of $\boldsymbol{E_1}$ and $\boldsymbol{E_2}$ lasers, respectively. The in-phase $\boldsymbol{E_{s1}}$ signal is generated by a combination of $\boldsymbol{E_1}$ and reflection $\boldsymbol{E_1'}$ under phase-matched condition ($\boldsymbol{k_1 + k_1' = k_S + k_{AS}}$). At the same time, the spectral signals from different energy levels with different lifetimes can be obtained through boxcar gated integrators which can be controlled from the time gate. The time gate can control the ratio of out of FL and $E_{S/AS}$.

Therefore, photon-phonon atomic coherence interaction can be controlled by changing the time gate, broadband/narrowband excitation, and thermal/phase transition phonon.

2.1. Theoretical Model

A. Photon-photon atomic coherence cross-interaction

The single laser or two lasers excitation shows photon dressing. Different lattice vibrations produced different frequency phonons. Such different frequency phonon can match to different crystal field splitting levels $^5D_1$-$^7F_1$, $^5D_0$-$^7F_1$, and $^5D_0$-$^7F_3$ in the ion Eu^{3+}, so more phonon results in effective dressing. The three sharp dips are hard to be explained only by photon field dressing. Therefore, phonon can be used to explain three sharp dips. The cross-interaction evolves from FL to hybrid (coexistence of second order FL and SFWM), to SFWM are below

$$|\rho_{F1}^{(2)} + \rho_{F2}^{(2)}|^2 = |\rho_{F1}^{(2)}|^2 + |\rho_{F2}^{(2)}|^2 + 2|\rho_{F1}^{(2)}||\rho_{F2}^{(2)}|\cos(\theta_F), \quad (1)$$

$$|\rho_{AS1}^{(3)} + \rho_{AS2}^{(3)}|^2 = |\rho_{AS1}^{(3)}|^2 + |\rho_{AS2}^{(3)}|^2 + 2|\rho_{AS1}^{(3)}||\rho_{AS2}^{(3)}|\cos(\theta_{AS}), \quad (2)$$

$$|\rho_H^X|^2 = |\rho_{F1}^{(2)} + \rho_{F2}^{(2)} + \rho_{S1}^{(3)} + \rho_{S2}^{(3)}|^2 . \quad (3)$$

When the laser field E_1 and E_2 are applied, the density matrix elements of out of phase FL for [H+M]-phase Eu^{3+}: $BiPO_4$ via perturbation chain $\rho_{11}^{(0)} \xrightarrow{E_1} \rho_{12}^{(1)} \xrightarrow{(E_1)^*} \rho_{22}^{(2)}$ and $\rho_{00}^{(0)} \xrightarrow{E_2} \rho_{20}^{(1)} \xrightarrow{(E_2)^*} \rho_{22}^{(2)}$ can be written as $\rho_{F1}^{(2)} = -|G_1|^2/((\Gamma_{12} + i\Delta_1 + |G_2|^2/(\Gamma_{02} + i(\Delta_1 - \Delta_2)))\Gamma_{22})$, $\rho_{F2}^{(2)} = -|G_2|^2/((\Gamma_{20} + i\Delta_2 + |G_1|^2/(\Gamma_{21} - i(\Delta_1 - \Delta_2)))\Gamma_{22})$. Where $\rho_{F1}^{(2)} = |\rho_{F1}^{(2)}|e^{i\theta_{F1}}$, $\rho_{F2}^{(2)} = |\rho_{F2}^{(2)}|e^{i\theta_{F2}}$, $\theta_F = \theta_{F1} - \theta_{F2}$. In Λ-type three-level system, the third-order density matrix elements $\rho_{AS}^{(3)}$ via $\rho_{11}^{(0)} \xrightarrow{E_1} \rho_{21}^{(1)} \xrightarrow{E_S} \rho_{22}^{(2)} \xrightarrow{E_1'} \rho_{20(AS)}^{(3)}$ can be written as $\rho_{AS}^{(3)} = -iG_S G_1 G_1' / ((\Gamma_{21} + i\Delta_1)(\Gamma_{22} + i\Delta_1 + |G_2|^2/(\Gamma_{20} + i\Delta_1 - i\Delta_2))(\Gamma_{20} + i\Delta_1 + i\Delta_1'))$. Where $\rho_{AS1}^{(3)} = |\rho_{AS1}^{(3)}|e^{i\theta_{AS1}}$, $\rho_{AS2}^{(3)} = |\rho_{AS2}^{(3)}|e^{i\theta_{AS2}}$, $\theta_{AS} = \theta_{AS1} - \theta_{AS2}$. The $\Gamma_{ij} = (\Gamma_i + \Gamma_j)/2$ is the transverse

Preprints (www.preprints.org) | NOT PEER-REVIEWED | Posted: 25 October 2022 doi:10.20944/preprints202210.0389.v1

decay rate, where $\Gamma_{i/j}=\Gamma_{pop}+\Gamma_{ion-spin}+\Gamma_{ion-ion}+\Gamma_{phonon}+\Gamma_{dressing}$. Γ_{phonon} is more related to broadband excitation.

In physics, the $\rho_{F1}^{(2)}$ generated from the field E_1 contains external field dressing $|G_2|^2$, and $\rho_{F2}^{(2)}$ from the field E_2 contains external field dressing $|G_1|^2$. So the $|\rho_{F1}^{(2)}+\rho_{F2}^{(2)}|^2$ shows photon2 and photon1 dressing cross-interaction of FL signal [16] at profile E_1/E_2 resonance in Figs. 3, 6 and 7. In Eqs. (2, 3), the $|\rho_{AS1}^{(3)}+\rho_{AS2}^{(3)}|^2$ and $\rho_{F1}^{(2)}+\rho_{F2}^{(2)}+\rho_{AS1}^{(3)}+\rho_{AS2}^{(3)}|^2$ are similar to the $|\rho_{F1}^{(2)}+\rho_{F2}^{(2)}|^2$ with two single external dressing. So, the $|\rho_{AS1}^{(3)}+\rho_{AS2}^{(3)}|^2$ (Figs. (4-7)) and $|\rho_H^X|^2$ (Fig. 7) show cross-interaction of SFWM and hybrid signals, respectively.

B. Photon-phonon atomic coherence self-interaction

The self-term $|\rho_{F2}^{(2)}|^2$ (or $|\rho_{F1}^{(2)}|^2$) is taken from in Eq. (1) with external dressing. The phonon1 dressing $|G_{p1}^T|^2$ and internal dressing $|G_2|^2$ (or $|G_1|^2$) are included in self-term $|\rho_{F2}^{\prime\prime(2)}|^2=|-|G_2|^2/((\Gamma_{20}+i\Delta_2+d_1)\Gamma_{00}|^2$ with broadband E_1 dressing (or $|\rho_{F1}^{\prime\prime(2)}|^2=|-|G_1|^2/((\Gamma_{12}+i\Delta_1+d_2)\Gamma_{22}|^2$ with broadband E_1 generation), where $d_1=|G_{p1}^T|^2/(\Gamma_{10}+i\Delta_2-i\Delta_{p1}^j)+|G_1|^2/(\Gamma_{21}+i\Delta_2-i\Delta_1)$ (or $d_2=|G_{p1}^T|^2/(\Gamma_{10}+i\Delta_1+i\Delta_{p1}^j)+|G_2|^2/(\Gamma_{02}+i\Delta_1-i\Delta_2)$). For example, the $|\rho_{F2}^{\prime\prime(2)}|^2$ with two cascade dressing is expanded as shown follows

$$|\rho_{F2}^{\prime\prime(2)}|^2=|\rho_{F2}^{(2)}+\rho_{F2}^{\prime(4)}+\rho_{F2}^{\prime\prime(4)}|^2. \quad (4)$$

The $|\rho_{F2}^{\prime\prime(2)}|^2$ and $|\rho_{F1}^{\prime\prime(2)}|^2$ contain $|\rho_{F2}^{\prime\prime(2)}|^2+2|\rho_{F1}^{\prime\prime(2)}||\rho_{F2}^{\prime\prime(2)}|\cos(\Delta\varphi_{F2})$ in Eq. (4) and $|\rho_{F1}^{\prime\prime(2)}|^2+2|\rho_{F1}^{\prime\prime(2)}||\rho_{F2}^{\prime\prime(2)}|\cos(\varphi_{F2})$, which show out of phase FL2 and FL1 self-interaction of two lasers, respectively. However, when the external field dressing is neglected at off-resonance, the Eq. (4) becomes one laser self-interaction of FL.

The photon1 exciting atomic coherence (Γ_{12} and ρ_{12}) between $|1\rangle$ and $|2\rangle$ couples to phonon1 atomic coherence by a common level $|1\rangle$ (Fig. 1(b)) in $|\rho_{F2}^{\prime\prime(2)}|^2$. The photon2 excites atomic coherence (Γ_{20} and ρ_{20}) between $|0\rangle$ and $|2\rangle$. By Taylor expansion for cascade dressing, the dressing (atomic coherence) coupling effect is transferred into the nonlinear generating process in Eq. (4). Thus, we obtain the generating Hamiltonian $H=i\hbar\kappa_F\alpha_1^\dagger\alpha_2^\dagger\alpha_{p1}^\dagger+H.c.$ for sixth-order nonlinearity, where $\kappa_F=-i\varpi_F\chi^{(6)}E_{FL}E_1E_2E_{p1}/2$. The ϖ_F is the central frequency of FL.

Next, the difference from the self-term $|\rho_{AS2}^{(3)}|^2$ (or $|\rho_{AS1}^{(3)}|^2$) in Eq. (2), the internal dressing $|G_2|^2$ (or $|G_1|^2$) and two phonon dressing ($|G_{p1}^T|^2$ and $|G_{p2}^T|^2$) are included in $\rho_{AS2}^{\prime\prime\prime\prime}$ (or $\rho_{AS1}^{\prime\prime\prime\prime}$). Where $\rho_{AS2}^{\prime\prime\prime\prime}=-iG_{S2}G_2G_2/d_1$ (or $\rho_{AS1}^{\prime\prime\prime\prime}=-iG_{S1}G_1G_1'/((\Gamma_{21}+i\Delta_1)d_5d_6)$),

$d=|G_2|^2/(\Gamma_{20}+i\Delta_1+|G_{p1}^T|^2/(\Gamma_{01}+i\Delta_1-i\Delta_{p1}^j+|G_{p2}^T|^2/(\Gamma_{31}+i\Delta_1-i\Delta_{p1}^j+\Delta_{p2}^j))$,

Preprints (www.preprints.org) | NOT PEER-REVIEWED | Posted: 25 October 2022 doi:10.20944/preprints202210.0389.v1

$d_1 = (\Gamma_{20} + i\Delta_2 + d + |G_1|^2 / (\Gamma_{21} + i\Delta_2 - i\Delta_1))(\Gamma_{22} + i\Delta_2)(\Gamma_{20} + 2i\Delta_2)$,

$d_2 = |G_1|^2 / (\Gamma_{21} + i\Delta_1 + |G_{p1}^T|^2 / (\Gamma_{01} + i\Delta_1 - i\Delta_{p1}^j + |G_{p2}^T|^2 / (\Gamma_{31} + i\Delta_1 - i\Delta_{p1}^j + \Delta_{p2}^j))$, $d_3 = |G_2|^2 / (\Gamma_{20} + i\Delta_2 + i\Delta_1)$,

$d_4 = \Gamma_{00} + i\Delta_1$, $d_5 = \Gamma_{20} + i\Delta_1' + i\Delta_1$, $d_6 = \Gamma_{22} + i\Delta_1 + d_2 + d_3$. The $|\rho_{AS2}^{\prime\prime\prime(3)}|^2$ with four cascade-nested dressing is expanded as shown follows

$$|\rho_{AS1}^{\prime\prime\prime\prime}|^2 = |\rho_{AS1}^{(3)} + \rho_{AS1}^{(5)} + \rho_{AS1}^{\prime(5)} + \rho_{AS1}^{(7)} + \rho_{AS1}^{(9)}|^2 . \quad (5)$$

The in-phase anti-Stokes $|\rho_{AS2}^{\prime\prime\prime\prime}|^2$ and $|\rho_{AS1}^{\prime\prime\prime\prime}|^2$ contain $|\rho_{AS2}^{\prime\prime\prime\prime(3)}|^2 + 2|\rho_{AS1}^{\prime\prime\prime\prime(3)}||\rho_{AS2}^{\prime\prime\prime\prime(3)}|\cos(\theta_{AS}^{\prime\prime\prime\prime})$ in Eq. (5) and $|\rho_{AS1}^{\prime\prime\prime\prime(3)}|^2 + 2|\rho_{AS1}^{\prime\prime\prime\prime(3)}||\rho_{AS2}^{\prime\prime\prime\prime(3)}|\cos(\theta_{AS}^{\prime\prime\prime\prime})$, which show anti-Stokes2 and anti-Stokes1 self-interaction of two lasers, respectively. When the external dressing is neglected at off-resonance, Eq. (5) becomes one laser self-interaction of anti-Stokes.

Phonon1 excites atomic coherence (Γ_{10} and ρ_{10}) between $|0\rangle$ and $|1\rangle$. Phonon2 excites atomic coherence (Γ_{31} and ρ_{31}) between $|1\rangle$ and $|3\rangle$ (Fig. 1(b)). In four nested-cascade dressing of $\rho_{S2}^{\prime\prime\prime\prime}$, the atomic coherence from nested coupling among photon1, phonon1 and phonon2, couples with atomic coherence of photon2 (Fig. 1(b)) in a cascaded manner. Similar to Eq. (4), the dressing coupling effect is transferred into the nonlinear generating process in Eq. (5). Thus, we also obtain the generating Hamiltonian can be written as $H_2 = i\hbar\kappa_{AS}\alpha_1^\dagger\alpha_2^\dagger\alpha_{p1}^\dagger\alpha_{p2}^\dagger + H.c.$ for ninth-order nonlinearity, where $\kappa_S = -i\varpi_{AS}\chi'^{(9)}E_{AS}E_S E_1 E_2 E_{p1}E_{p2}/2$. The ϖ_{AS} is the central frequency of anti-Stokes.

C. Simulation of non-linear signals dressing interaction

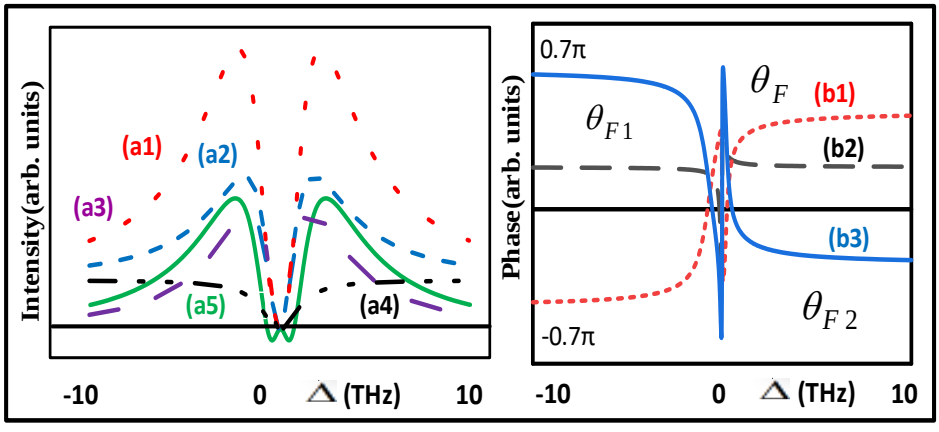

Fig. 2 (a1) The total signal intensity of $|\rho_{F1}^{(2)}|^2 + |\rho_{F2}^{(2)}|^2$ (hot curve), (a2) $|\rho_{F1}^{(2)}|^2$ (blue curve), (a3) the interaction item $2|\rho_{F1}^{(2)}||\rho_{F2}^{(2)}|\cos(\theta)$ versus Δ (purple curve), (a4) $|\rho_{F2}^{(2)}|^2$ (black curve), (a5) $|\rho_{sum}^{(2)}|^2$ (green curve). Fig. 2(b) Here $\Delta = \Delta_1 - \Delta_2$, $\theta = \theta_{F1} - \theta_{F2}$ .The parameters are $G_1 = 2.3$ THz, $G_2 = 6.1$ THz. (b1) θ (hot curve), (b2) θ_{F1} (black curve), (a3) θ_{F2} (blue curve)

Preprints (www.preprints.org) | NOT PEER-REVIEWED | Posted: 25 October 2022 doi:10.20944/preprints202210.0389.v1

versus Δ . Evolution of θ_F , the constructive and the destructive interaction versus Δ . Fig. 2(b) The destructive or constructive interaction is studied in this system [23].

Figure 2(a) shows FL1 and FL2 self-terms $|\rho_{F1}^{(2)}|^2+|\rho_{F2}^{(2)}|^2$, cross-term $2|\rho_{F1}^{(2)}||\rho_{F2}^{(2)}|\cos(\theta_F)$ in cross-interaction of two lasers $|\rho_{sum}^{(2)}|^2$ at $\Delta_1=\Delta_2/2$ versus the detuning difference $\Delta=\Delta_1-\Delta_2$ from Eq. (1). $|\rho_{F1}^{(2)}|^2$ and $|\rho_{F2}^{(2)}|^2$ have the maximal values at $\Delta=\pm4.1$ THz and $\Delta=\pm3.6$ THz, respectively. Hence, there exist two peaks at around $\Delta=\pm10$ THz in the hot curve that represents the cross-interaction $|\rho_{sum}^{(2)}|^2$. The purple curve shows the cross-term $2|\rho_{F1}^{(2)}||\rho_{F2}^{(2)}|\cos(\theta_F)$. Here the value below or above zero suggests destructive or constructive interference, respectively. In fact, variations of the phase difference between second-order FL1 and FL2 change constructive interaction into destructive interaction, and vice versa. Furthermore, $\rho_{F1}^{(2)}=|\rho_{F1}^{(2)}|e^{i\theta_{F1}}$ and $\rho_{F2}^{(2)}=|\rho_{F2}^{(2)}|e^{i\theta_{F2}}$, we get $|\rho_{F1}^{(2)}+\rho_{F1}^{(2)}|^2-|\rho_{F1}^{(2)}|^2-|\rho_{F2}^{(2)}|^2=2|\rho_{F1}^{(2)}||\rho_{F1}^{(2)}|\cos(\theta_F)$ from Eq. (1). Figure 2(b) shows the phases θ_{F1}, θ_{F2}, and the phase difference θ versus Δ. As the θ_{F1} and θ_{F2} are changed, the θ_F alternates between -0.7π and 0.7π. The interaction switches from constructive ($[-0.5\pi,0.49\pi)$), destructive ($[-0.7\pi,0.5\pi)$), constructive ($[-0.5\pi,0.5\pi)$), and destructive ($[0.5\pi,0.7\pi)$) and constructive ($[0.49\pi,0.5\pi)$). In a word, our simulation (Fig.2) is obtained by scanning $\Delta=\Delta_2-\Delta_1$ [23], and our experiment result (Figs. (3-7)) is gained by scanning the dressing field Δ_2 .For simplicity, we only considered the external dressing in simulation (Eq. (1)). Furthermore, Eqs. (1-3) reveals the cross-interaction of two lasers. If the internal dressing and phonon dressing are considered, the cross-interaction become complicated.

2.2. Experiments

Photon excitation atomic coherence between different states ($^5D_0$ and $^7F_1$) can be coupled to phonon excitation atomic coherence in the same state ($^7F_1$). Unlike photon atomic coherence of crystal field splitting with different states, the phonon atomic coherence of crystal field splitting in the same state is difficult to optically excite.

Moreover, the phonon dressing can control destructive and constructive interaction. The constructive interaction results from less phonon dressing (77K, M-phase, narrowband E_2), whereas the destructive interaction is caused by more phonon dressing (300K, H-phase, broadband E_1).

A. FL dressing cross- and self-interaction

Figures (3-7) shows the connected spectrum of dressing cross-interaction of two lasers with different bandwidth. The spectrum profile of such interactions can be achieved by connecting several spectrums together by scanning Δ_2/Δ_1 at different detuning (Δ_1/Δ_2) and can be written as $|\rho_{F/AS1}+\rho_{F/AS2}|^2=R_1(\theta_{F/AS})+N_1(\theta_{F/AS})=R_2(\theta_{F/AS})+N_2(\theta_{F/AS})$. When the Δ_i (i=1, 2) is scanned, the R_i and N_i shows resonance and non-resonance profile term,

Preprints (www.preprints.org) | NOT PEER-REVIEWED | Posted: 25 October 2022 doi:10.20944/preprints202210.0389.v1

respectively. The broad peak ($N_i(\theta_{F/AS}=0)$ profile) and broad dip ($N_i(\theta_{F/AS}=\pi)$ profile) in Figs. (3-7) show constructive and destructive interaction, respectively.

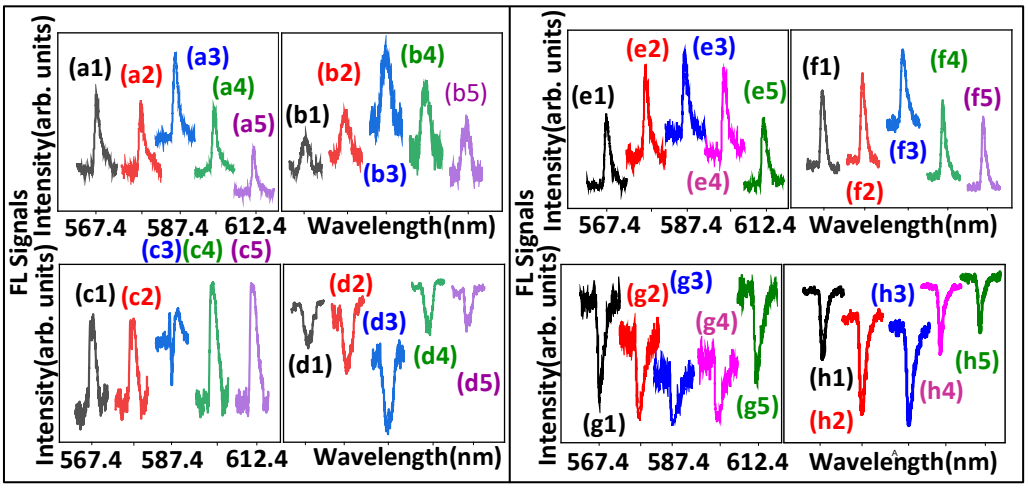

Fig. 3 (a, c) show self- and cross- interaction of FL observed from Eu^{3+} doped $BiPO_4$ [molar ratio (6:1)] at different E_1 wavelengths (567.4nm, 584.4nm, 587.4nm, 589.4nm, 612.4nm) and E_2 scanned from 567.4nm to 607.4nm at PMT1(far detector position) and PMT2 (near detector position), respectively. Figures 3(b, d) show self- and cross- interaction of FL at different E_2 wavelengths (567.4nm, 587.4nm, 588nm, 588.4nm, 602.4nm) and E_1 scanned from 567.4nm to 612.4nm. Figures 3(e-h) show spectral signal intensity for (1:1) sample, which is same condition as Figs. 3(a-d). The time gate = 1μs.

Figures 3(a, b, e, f) show the constructive cross-interaction of FL (sharp peak $R_i(\theta_F=0)$, broad peak $N_i(\theta_F=0)$ (profile)) at E_1/E_2 resonance. When the time gate is fixed at 1μs, the FL emission is turn out to be dominant. The increasing sharp peaks at E_1 $N_2(\theta_F=0)$ (Figs. 3(a3, e3) and E_2 $N_1(\theta_F=0)$ (Figs. 3(b3, f3) resonance come from constructive cross-interaction due to $|\rho_{F1}^{(2)}+\rho_{F2}^{(2)}|^2$ from Eq. (1). Such increasing sharp peak comes from the (6:1) sample and recorded at far detector position. Moreover, the broad peaks $N_i(\theta_F=0)$ in Figs. 3(a, e) and 3(b, f) come from single dressing constructive cross-interaction $N_1(\theta_F=0)$ and $N_2(\theta_F=0)$, respectively, which agrees with two single external dressing simulations illustrated in Fig. 2(a3). The sharp peaks at E_1 (Figs. 3(a, e) and E_2 (Figs. 3(b, f) off-resonance result from self-interaction with internal dressing $|G_2|^2$ and $|G_1|^2$, respectively.

Figure 3(c) shows the cross-interaction of FL (sharp dip $R_2(\theta_F''=\pi)$) and broad peak $N_2(\theta_F''=0)$) at E_1 resonance. Compared with the sharp peak (Fig. 3(c)) at E_1 off-resonance, the dressing small dip $R_2(\theta_F''=\pi)$ at E_1 resonance (Fig. 3(c3)) results from the switch of two cascade dressing (external photon $|G_1|^2$ and phonon1 $|G_{p1}^{T1}|^2/(\Gamma_{10}+i\Delta_{p1}^c)+|G_1|^2/(\Gamma_{20}+i\Delta_1)$ in Eq. (4)). Moreover, the sharp peak $R_2(\theta_F=0)$ at E_1 resonance (Fig. 3(a3)) is transferred into a small dip $R_2(\theta_F'=\pi)$ in Fig. 3(c3) due to phonon1 dressing $|G_{p1}^{T1}|^2/(\Gamma_{10}+i\Delta_{p1}^c)$ at near detector position (broadband FL). Similar to

Preprints (www.preprints.org) | NOT PEER-REVIEWED | Posted: 25 October 2022 doi:10.20944/preprints202210.0389.v1

Figs. 3(a, b, e, f), the broad peak in Fig. 3(c) results from constructive cross-interaction $N_2(\theta_F'=0)$ with less phonon dressing.

Figures 3(d, g, h) show destructive cross-interaction of FL (sharp dressing dip $R_i(\theta_F''=\pi)$), broad dip $N_i(\theta_F''=\pi)$ (profile)) at E_1 resonance. Compared with the sharp dip at E_2 off-resonance from destructive self-interaction (Fig. 3(d)), the sharp dip at E_2 resonance (Fig. 3(d3)) increases due to the destructive cross-interaction $R_1(\theta_F''=\pi)$ with external dressing $|G_2|^2$ of $\rho_{F1}''^{(2)}$ in $|\rho_{F1}''^{(2)}+\rho_{F2}^{(2)}|^2$ at broadband excitation E_1 and 300K. Because, the more crystal field splitting levels $^7F_1$ (Fig. 1(b)) and lattice vibrations are coupled by broadband excitation E_1. Moreover, the 300K result in more thermal phonons with large G_{p1}^{T1}. The broad dip (Fig. 3(d)) comes from stronger destructive cross-interaction $N_1(\theta_F''=\pi)$ with more phonon dressing. The sharp dressing dips at E_2 off-resonance (Fig. 3(d)) come from the self-interaction from Eq. (4).

The sharp dips at E_1 off-resonance come from phonon1 dressing $|G_{p1}^{T1}|^2/(\Gamma_{10}+i\Delta_{p1}^c)$ of $\rho_{F1}''^{(2)}$ shown in Fig. 3(d). The sharp dip $R_1(\theta_F''=\pi)$ at E_1 resonance results from cascade dressing $|G_2|^2+|G_{p1}|^2/(\Gamma_{10}+i\Delta_2+i\Delta_{p1}^d)$ of $\rho_{F1}''^{(2)}$ shown in Fig. 3(d3). Such cascade dressing coupling results in photon1-phonon2-phonon1 ($\alpha_1^\dagger$, $\alpha_2^\dagger$, $\alpha_{p1}^\dagger$ in $\chi^{(6)}$) atomic coherence coupling.

Figure 3(g) corresponds to the simulation (Fig. 5(g)) modelled through Eq. (4). Compared with the sharp dip at E_1 off-resonance (Fig. 3(g)), the sharp dip at E_1 resonance (Fig. 3(g3)) decreases due to the cross-interaction $R_2(\theta_F''=\pi)$ with phonon1 dressing $|G_{p1}^{T1}|^2/(\Gamma_{10}+i\Delta_{p1}^d)+|G_1|^2$ from Eq. (4) at narrowband excitation. The broad dip in Fig. 3(g) comes from strong destructive cross-interaction $N_2(\theta_F''=\pi)$ with more phonon dressing. Similar to Fig. 3(d), the broad dip (Fig. 3(h)) can be explained by stronger destructive cross-interaction $N_1(\theta_F''=\pi)$ with phonon1 dressing $|G_{p1}^{T1}|^2/(\Gamma_{10}+i\Delta_{p1}^d)+|G_2|^2$ of $\rho_{F1}''^{(2)}$. Compared with small dip at E_1 resonance (Fig. 3(c3)), the large dip is shown in Fig. 3(g3) due to phase transition phonon dressing $|G_{p1}^{T1}|^2/(i\Delta_{p1}^c+i\Delta_1)\lhd|G_{p1}^{T1}|^2/(i\Delta_{p1}^d+i\Delta_1)$. Such phonon dressing dip results from resonance detuning Δ_{p1}^d ($\Delta_{p1}^d<\Delta_{p1}^c$), which is due to high phonon frequencies ω_{p1}^d ($\omega_{p1}^d>\omega_{p1}^c$) for H-phase samples (6:1, 1:1) in Figs. 3(d, h).

The transistor as a peak amplifier1 and dip amplifier2[24] shown in Fig. 1(d) is realized from spectral results observed in Figs. 3(b) and 3(d). In our proposed model, the FL signal is input (a_{in} =FL); E_2 is a control signal (analogous to the base current of BJT), while a_{out} is the output of the

Preprints (www.preprints.org) | NOT PEER-REVIEWED | Posted: 25 October 2022 doi:10.20944/preprints202210.0389.v1

transistor, and transistor gain (g) is related to external dressing effect and can be controlled through detuning of E_2 beam. First, when E_2 is set at off-resonance ($\Delta_2 \neq 0$), the amplitude of both sharp peak (Fig. 3(b1)) and sharp dip (Fig. 3(d1)) is very low. When detuning of E_2 approaches resonance ($\Delta_2 = 0$), the amplitude of both sharp peak (Fig. 3(b3)) and dip (Fig. 3(d3)) amplifies by a factor of three. The amplification of spectral signals can be explained from high gain (g>>1) caused by strong external dressing $|G_2|^2$ at resonance wavelength.

Next, we extend our research and study the cross-interaction of SFWM in the following section **B.**

B. SFWM dressing cross- and self-interaction

The out of phase FL (time gate=1μs) interaction is transferred to in-phase SFWM interaction (time gate=500μs). When the time gate is increased to 5μs, SFWM signal (sharp R_i) is dominant.

Figures 4(a) show the constructive cross-interaction of SFWM (two sharp peaks $R_1(\theta_{AS}=0)$, broad peak $N_1(\theta_{AS}=0)$ (profile)) at E_1 resonance. Compared with two sharp peaks at E_2 off-resonance (Fig. 4(a)), the two sharp peaks (Fig. 4(a3)) at E_2 resonance also increase due to constructive interaction $R_1(\theta_{AS}=0)$ with $|\rho_{AS1}^{(3)}+\rho_{AS2}^{(3)}|^2$ in Eq. (2). Such two sharp peaks can be explained by crystal filed splitting levels ($|1\rangle$,$|0\rangle$) due to high resolution of in-phase SFWM. The broad peak comes from cross-interaction $N_1(\theta_{AS}=0)$ in Fig. 4(a).

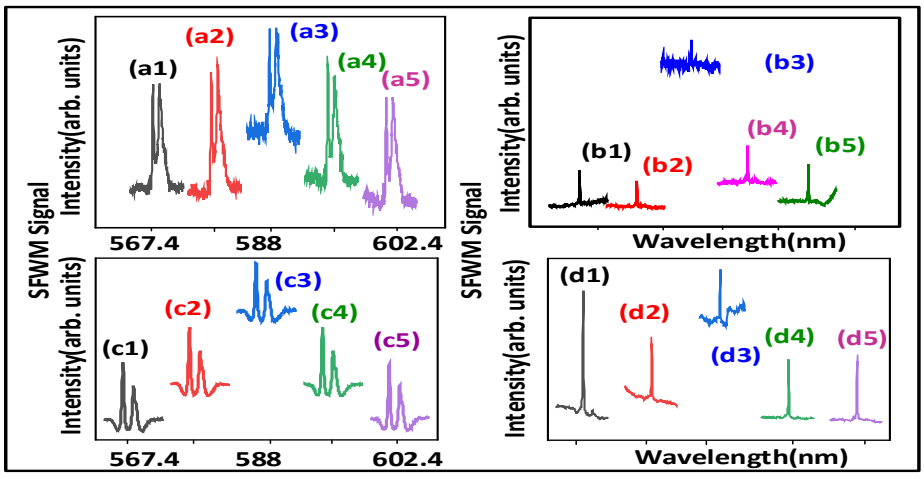

Fig. 4 (a1-a5, b1-b5) show SFWM cross-interaction observed from Eu^{3+} doped $BiPO_4$ [molar ratio (7:1)] at different narrowband laser E_2 (567.4nm, 587.4nm, 588nm, 588.4nm, 602.4nm) while broadband laser E_1 is scanned from 572.4nm to 612.4nm at different broadband laser E_1 wavelengths (567.4nm, 584.4nm, 587.4nm, 596.4nm, 612.4nm) and narrowband laser E_2 is scanned from 567.4nm to 607.4nm at 300K, respectively at PMT1. The time gates are 5μs and 20μs, respectively, gate width=400ns. Figure 4(c, d) shows SFWM cross-interaction for the (20:1) sample at the time gate =10μs and 20μs, respectively. The other experimental condition is the same as Figs. 4(a, b), respectively at PMT1.

Preprints (www.preprints.org) | NOT PEER-REVIEWED | Posted: 25 October 2022 doi:10.20944/preprints202210.0389.v1

Figures 4(b, d) show the constructive cross-interaction of SFWM (single sharpest peak $R_2(\theta'_{AS}=0)$, broad peak $N_2(\theta'_{AS}=0)$) at E_1 resonance. Compared with the sharpest peak at E_1 off-resonance (Fig. 4(b)), the amplitude of sharpest peak $R_2(\theta'_{AS}=0)$ at E_1 resonance (Fig. 4(b3)) decreases due to constructive cross-interaction with phonon1-assisted G_2 dressing (G_{p1}^{T2} and G_2 share the common atomic coherence) $(|G_1|^2+|G_{p1}^T|)^2/(\Gamma_{10}+i\Delta_1+i\Delta_{p1}^a)$ of $\rho'^{(3)}_{AS2}$. Compared with sharp peak (Fig. 4(a3)), the linewidth of such sharpest peak decreases due to less thermal phonon (77K) with small G_{p1}^{T2}. The broad peak comes from constructive interaction $N_2(\theta'_{AS}=0)$ in Fig. 4(b) with less phonon dressing. However, the sharpest peak (Fig. 4(b)) at E_1 off-resonance is due to self-interaction.

Figure 4(c) shows the constructive cross-interaction of SFWM (two sharp peaks $R_1(\theta''_{AS}=0)$, broad peak $N_1(\theta''_{AS}=0)$) at E_2 resonance. The proportion of the two sharp peaks accounts for roughly of 80% and the proportion of single sharp dips only accounts for roughly of 20% in Fig. 4(c). Compared with two sharp peaks at E_2 off-resonance in Fig. 4(c), such two sharp peaks (Fig. 4(c3)) at E_2 resonance decrease due to constructive cross-interaction $R_1(\theta''_{AS}=0)$. The broad peak comes from constructive interaction $N_1(\theta''_{AS}=0)$ in Fig. 4(c). The small sharp dip (Fig. 4(c3)) at E_2 resonance is obtained from destructive cross-interaction due to phonon1 dressing $|G_{p1}^T|^2/(\Gamma_{10}+i\Delta_2+i\Delta_{p1}^b)+|G_2|^2$ in Eq. (5).

Compared with two sharp peaks at E_2 resonance for the (7:1) sample (Fig. 4(a3)), the small sharp dip at E_2 resonance is shown in Fig. 4(c3)) due to phonon dressing ($\Delta_{p1}^a>\Delta_{p1}^b$, $|G_{p1}^{T2}|^2/i\Delta_{p1}^a \lhd |G_{p1}^{T2}|^2/i\Delta_{p1}^b$) for more H-sample (20:1). Such small sharp dip result from the switch of two cascade dressing (external photon $|G_2|^2$ and phonon1 $|G_{p1}^{T1}|^2/(\Gamma_{10}+i\Delta_{p1}^b)+|G_2|^2$ of $\rho'^{(3)}_{AS1}$). Because the phonon dressing is easily distinguished by in-phase SFWM.

Similar to Fig. 4(b3), the sharpest peak at E_1 resonance also decreases due to constructive cross-interaction $R_2(\theta'_{AS}=0)$ with phonon1-assisted dressing in Fig. 4(d3).

Figures 5(a) show the constructive cross-interaction of SFWM (sharp peak $R_2(\theta_{AS}=0)$), and broad peak $N_2(\theta_{AS}=0)$) at E_1 resonance. Similar to Figs. 4(b, d), the sharp peak (Fig. 5(a3)) at E_1 resonance decreases as compared to the sharp peaks at E_1 off-resonance (Fig. 5(a)) due to cross-interaction $R_2(\theta_{AS}=0)$ with phonon1-assisted dressing $(|G_1|^2+|G_{p1}^{T1}|)^2/(\Gamma_{10}+i\Delta_1+i\Delta_{p1}^c)$ of $\rho'^{(3)}_{AS2}$. The broad peak at E_1 off-resonance comes from constructive interaction $R_2(\theta_{AS}=0)$ due to less phonon dressing.

Preprints (www.preprints.org) | NOT PEER-REVIEWED | Posted: 25 October 2022 doi:10.20944/preprints202210.0389.v1

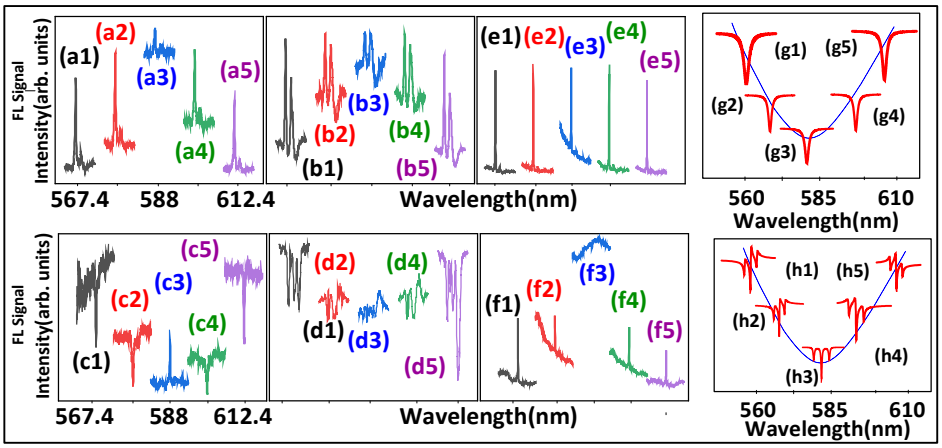

Fig. 5 (a, c) show SFWM cross- interaction observed from Eu^{3+} doped in molar ratio (6:1) $BiPO_4$ at different E_1 wavelengths (567.4nm, 584.4nm, 588.4nm, 596.4nm, 612.4nm) and E_2 scanned from 567.4nm to 607.4nm at PMT1 and PMT2 at 300K, respectively. (b, d) shows SFWM cross- interaction at different E_2 wavelengths (567.4nm, 587.4nm, 588nm, 588.4nm, 602.4nm) and E_1 scanned from 567.4nm to 612.4nm at PMT1 and PMT2 in 300K, respectively. (e, f) shows SFWM cross-interaction at 77K. The other experimental conditions are same as Figs. 5(a, c), respectively. Time gate = 500μs. Figures. 5(g1-g5) show the simulation result corresponding to Figs. 5(b1-b5). Figures. 5(h1-h5) show the simulation result corresponding to Figs. 3(g1-g5) and 7(e1-e5).

Figures 5(b) show the constructive cross-interaction of SFWM (two sharp peaks $R_1(\theta''_{AS}=0)$, broad peak $N_1(\theta''_{AS}=0)$) at E_2 resonance. Compared with the small dip at E_2 resonance (Fig. 4(c3)), the small dip at E_2 resonance (Fig. 5(b3)) increases due to cross-interaction $R_1(\theta''_{AS}=0)$ with phonon1 dressing $|G_{p1}^{T1}|^2/(\Gamma_{10}+i\Delta_2+i\Delta_{p1}^c)$ in Eq. (5). Such small sharp dip results from the switch of two cascade dressing $|G_{p1}^{T1}|^2/(\Gamma_{10}+i\Delta_{p1}^c)+|G_2|^2$ of $\rho''^{(3)}_{AS1}$. The broad peak in Fig. 5(b) comes from constructive cross-interaction $N_1(\theta''_{AS}=0)$ due to less phonon dressing.

Figures 5(c) show the cross-interaction of SFWM (sharp peak $R_2(\theta'''_{AS}=0)$, broad dip $N_2(\theta'''_{AS}=0)$ (profile)) at E_1 resonance. The sharp dip at E_1 off-resonance (Fig. 5(c)) is transferred into the sharp peak at E_1 resonance (Fig. 5(c3)) due to constructive cross-interaction $R_2(\theta'''_{AS}=0)$ with phonon1 dressing $|G_{p1}^{T1}|^2+|G_1|^2$ of $\rho''^{(3)}_{AS1}$ at narrowband excitation. Such transition (sharp dip $R_2(\theta'''_{AS}=\pi)$ to sharp peak $R_2(\theta'''_{AS}=0)$) results from the switch of three cascade dressing (internal photon G_2, external photon G_1 and phonon1 G_{p1} of $|G_{p1}^{T1}|^2/(\Gamma_{10}+i\Delta_{p1}^c)+|G_1|^2+|G_2|^2$ in $|\rho^{(3)}_{AS1}+\rho'''^{(3)}_{AS2}|^2$). The broad dip comes from strong constructive interaction $N_1(\theta'''_{AS}=\pi)$ in Fig. 5(c) with more phonon dressing. More interestedly, the sharp dips at E_1 off-resonance (Fig. 5(c)) result from self-interaction in Eq. (5). Such sharp dips are obtained from 300K due to more thermal phonon dressing (large G_{p1}^{T1}). Compared with the sharpest peak at E_1 off-

Preprints (www.preprints.org) | NOT PEER-REVIEWED | Posted: 25 October 2022 doi:10.20944/preprints202210.0389.v1

resonance for (7:1) and (20:1) sample (Fig. 4(c, d)), the sharp dip at E_1 off-resonance (Fig. 5(c)) decreases due to phase transition phonon dressing ($|G_{p1}^{T1}|^2/i\Delta_{p1}^{c} > |G_{p1}^{T2}|^2/i\Delta_{p1}^{a,b}$) for (6:1) more H-phase sample.

Figures 5(d) show the destructive cross-interaction of SFWM (three sharp dips $R_1(\theta_{AS}''''=\pi)$, broad dip $N_1(\theta_{AS}''''=\pi)$) at E_2 resonance. Difference with three sharp dips at E_2 off-resonance from destructive self-interaction (Eq. (5)) in Fig. 5(d), the three sharp dips at E_2 resonance in Fig. 5(d3) result from destructive cross-interaction $R_1(\theta_{AS}''''=\pi)$ with phonon1 and phonon2 dressing. The broad dip in Fig. 5(d) is obtained from stronger destructive cross-interaction $N_1(\varphi_{AS}''''=\pi)$ with more phonon dressing at 300K and broadband excitation. Figure 5(d) corresponds to the simulation result (Fig. 5(h)) from Eq. (5).

The three sharp dips at E_2 off-resonance (Fig. 5(d)) result from three nested dressing (internal photon G_1 , two phonons). However, the decreasing three sharp dips $R_1(\theta_{AS}''''=\pi)$ at E_2 resonance (Fig. 5(d3)) come from external dressing $|G_2|^2$ of four nested-cascade dressing (internal photon G_1 , external photon G_2 and two phonons) $|G_1|^2/(\Gamma_{20}+|G_{p1}^{T1}|^2/(\Gamma_{10}-i\Delta_{p1}^{c}+|G_{p2}^{T1}|^2/(\Gamma_{13}-i\Delta_{p1}^{c}-i\Delta_{p2}^{c})))+|G_2|^2$ of $\rho_{AS1}''''^{(3)}$ (Eq. (5)) in $|\rho_{AS2}^{(3)}+\rho_{AS1}''''^{(3)}|^2$. Such four dressing coupling results from photon1-phonon2-phonon1-phonon2 ($\alpha_1^{\dagger},\alpha_2^{\dagger},\alpha_{p1}^{\dagger},\alpha_{p2}^{\dagger}$ in $\chi^{(9)}$) atomic coherence coupling.

The more phonon dressing result from more lattice vibrations at 300K for Eu^{3+}: $BiPO_4$ than other samples (Eu^{3+}/Pr^{3+}: YPO_4 [24] and Pr^{3+}: Y_2SO_5 [25]). The model for phonon-controlled transistor switch is presented in Fig. 1(d) where 'enhancement peak' and 'suppression dip' corresponds to 'ON-state' and 'OFF-state', respectively. When the input signal (Fig. 3(b3)) is in single ON-State (higher than baseline) then the corresponding output signal (Fig. 3(d3)) is at single OFF-State (lower than baseline). Such spectral switch can be controlled by single phonon dressing ($|G_{p1}|^2$). Our experiment result defined the switching contrast as $C=(I_{off}-I_{on})/(I_{off}+I_{on})$, where I_{off} is the intensity at the OFF-state and I_{on} is the intensity at the ON-state. The maximum switching contrast C for single state switch is about 82% in Fig.3(b3) and 3(d3). Furthermore, when the ON-state of input signal is observed with two sharp peaks (Fig. 5(b3)) the corresponding output signal has OFF-state with three sharp dips as observed in Fig. 5(d3). Such multi-states switch can be controlled by two phonon dressing ($|G_{p1}|^2$, $|G_{p2}|^2$). The switching contrast C is about 93.6% for multi-states switch measure for Figs. 5(b3) and Fig. 5(d3).

Figures 5(e, f) show the constructive cross-interaction of SFWM (single sharpest peak $R_2(\theta_{AS}'=0)$, broad peak $N_2(\theta_{AS}'=0)$) at E_1 resonance. Compared with the sharpest peaks at E_1 off-resonance in Fig. 5(e), the sharpest peak $R_2(\theta_{AS}'=0)$ at E_1 resonance in Fig. 5(e3) increases due to constructive cross-interaction with phonon1-assisted dressing

Preprints (www.preprints.org) | NOT PEER-REVIEWED | Posted: 25 October 2022 doi:10.20944/preprints202210.0389.v1

$(|G_1|^2+|G_{p1}^{T2}|)^2/(\Gamma_{10}+i\Delta_1+i\Delta_{p1}^c)$ of $\rho_{AS2}'^{(3)}$ at 77K. Figure 5(g) shows simulation results corresponding to experimental result (Fig. 5(b)). The transition from broad dip $N_2(\theta_{AS}'=\pi)$ (Fig. 5(c)) to broad peak $N_2(\theta_{AS}'=0)$ (Fig. 5(f)) is due to the reduction of phonon dressing. So, thermal phonon dressing plays a key role in cross-interaction.

In order to explore more, we further compare the FL and SFWM interaction in section **C**.

C. Comparison of FL and SFWM interaction

The cross-interaction in Figs. 6-7 evolves from out of phase FL to hybrid (coexistence of second order FL and SFWM), to in-phase SFWM by changing the time gate (1μs to 500μs) obtained from (0.5:1) sample.

Figures 6(a-b) show the constructive cross-interaction of FL (sharp peak $R_1(\theta_F=0)$, broad peak $N_1(\theta_F=0)$) at E_2 resonance. Similar to Fig. 3(a3, b3, e3, f3), the increasing sharp peaks (Fig. 6(a3)) at E_2 resonance is due to constructive cross-interaction $R_1(\theta_F=0)$ in Eq. (1). Compared with sharp peak at E_2 off-resonance (Fig. 6(b)), the sharp peak $R_1(\theta_F=0)$ at E_2 resonance (Fig. 6(b3)) decreases due to phonon1-assisted dressing $(|G_2|^2+|G_{p1}^{T1}|)^2/(\Gamma_{10}+i\Delta_2+i\Delta_{p1}^e)$ of $\rho_{F1}'^{(3)}$ (similar to Fig. 5(a)).

Figures 6(c-d) show the constructive cross-interaction of SFWM (two sharpest peaks $R_1(\theta_{AS}'=0)$, broad peak $N_1(\theta_{AS}'=0)$) at E_2 resonance. When the time gate increases to 500μs, compared with two sharpest peaks at E_2 off-resonance in Figs. 6(c, d), two sharpest peaks $R_1(\theta_{AS}'=0)$ at E_2 resonance in Figs. 6(c3, d3) decreases due to phonon1-assisted dressing $(|G_2|^2+|G_{p1}^{T2}|)^2/(\Gamma_{10}+i\Delta_2+i\Delta_{p1}^e)$ in $\rho_{AS1}'^{(3)}$ (similar to Figs. 4(c3) and 5(a3)). The spectral linewidth of sharp peak in Fig. 6(a1) at 300K is 9 times larger than the linewidth at 77K in Fig. 6(c1) due to more thermal phonon dressing ($|G_{p1}^{T1}|^2/i\Delta_{p1}^e > |G_{p1}^{T2}|^2/i\Delta_{p1}^e$).

Similar to sharp peak with (6:1) sample at 300K (large G_{p1}^{T1}) in Figs. 5(a, b), the two sharpest peaks with (0.5:1) sample are also shown at 77K (small G_{p1}^{T2}) in Figs. 6(c, d) due to phase phonon dressing $|G_{p1}^{T2}|^2/(i\Delta_{p1}^e+i\Delta_1)$ from resonance detuning ($\Delta_{p1}^e\approx 0$). Therefore, compared with out of phase FL (Figs. 6(a, b)), in-phase SFWM is more sensitive to phonon dressing (Figs. 6(c, d)).

Preprints (www.preprints.org) | NOT PEER-REVIEWED | Posted: 25 October 2022 doi:10.20944/preprints202210.0389.v1

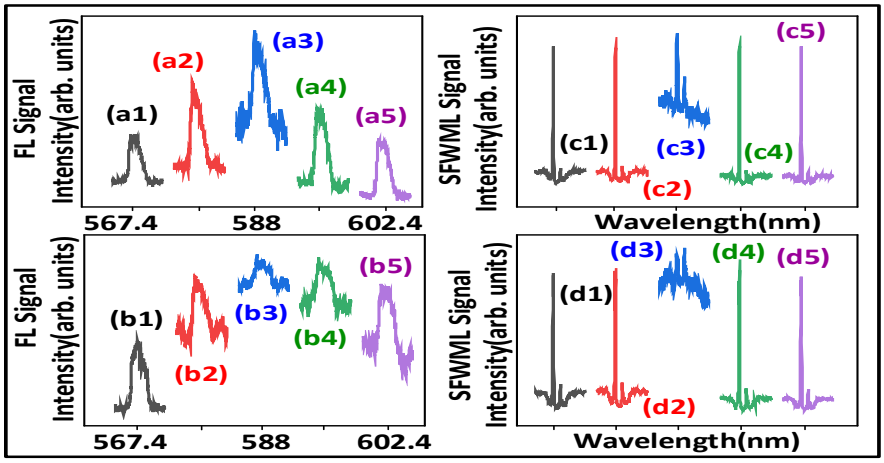

Fig. 6 (a, b) show FL cross-interaction observed from the output signals of Eu^{3+} doped in molar ratio (0.5:1) $BiPO_4$ at different E_2 wavelengths (567.4nm, 587.4nm, 588nm, 588.4nm, 602.4nm) and E_1 scanned from 572.4nm to 612.4nm at 300K, at PMT1 and PMT2, respectively. The time gate is 10μs. Figures 6(c, d) show SFWM cross-interaction at 77K at the time gate = 800μs, respectively. The other experimental condition is the same as Figs. 6(a, b).

Figures 7(a, b) show the constructive cross-interaction of FL (sharp peak $R_2(\theta_F = 0)$, broad peak $N_2(\theta_F = 0)$) at E_1 resonance. When the time gate is fixed at 1μs, compared with sharp peak at E_1 off-resonance in Fig. 7(a), the sharp peak $R_2(\theta_F = 0)$ at E_1 resonance in Fig. 7(a3) increases (similar to Fig. 6(a)). The sharp peak $R_2(\theta_F = 0)$ at E_1 resonance in Fig. 7(b3) decreases as compare to the sharp peaks at E_1 off-resonance in Fig. 7(b) due to phonon1-assisted dressing $(|G_1| + |G_{p1}^{T1}|)^2 / (\Gamma_{21} + i\Delta_1 + i\Delta_{p1}^e)$ of $\rho_{F2}^{\prime(2)}$.

Figures 7(c, d) show the constructive cross-interaction of hybrid (single sharpest peak R_2, broad peak N_2) at E_1 resonance. When the time gate increases to 100μs, difference with the sharpest peak at E_1 off-resonance in Figs. 7(c, d), the sharpest peaks R_2 at E_1 resonance in Figs. 7(c3, d3) decrease due to constructive cross-interaction with phonon1-assisted dressing of R_2 in Eq. (3). The broad peaks N_2 in Figs. 7(c, d) can be explained by constructive cross-interaction with less phonon dressing.

Figure 7(e) shows the destructive cross-interaction of SFWM (single sharpest dips $R_2(\theta''_{AS} = \pi)$, broad dip $N_2(\theta''_{AS} = \pi)$) at E_1 resonance. When the time gate reaches to 500μs, difference with sharpest dip at E_1 off-resonance, the sharpest dip $R_2(\theta''_{AS} = \pi)$ at E_1 resonance in Fig. 7(e3) decreases due to stronger destructive cross-interaction with phonon1 dressing. Such decreasing sharpest dip $R_2(\theta''_{AS} = \pi)$ results from external dressing $|G_1|^2$ of two cascade dressing $|G_{p1}^{T1}|^2 / (\Gamma_{10} + i\Delta_{p1}^d) + |G_1|^2$ in $\rho_{AS2}^{\prime\prime(3)}$. Moreover, the broad dip $N_2(\theta''_{AS} = \pi)$ is obtained from 300K and (0.5:1) sample with more phonon dressing.

Preprints (www.preprints.org) | NOT PEER-REVIEWED | Posted: 25 October 2022 doi:10.20944/preprints202210.0389.v1

Similar to Fig. 5(c), figure 7(f) shows the cross-interaction of SFWM (single sharpest peak $R_2(\theta''_{AS}=0)$, broad dip $N_2(\theta''_{AS}=\pi)$ at E_1 resonance. Difference with sharp dip at E_1 off-resonance in Fig. 7(f), the sharpest peak at E_1 resonance is shown in Fig. 7(f3) due to constructive cross-interaction $R_2(\theta''_{AS}=0)$ with less phonon dressing. Such transition (sharpest dip $R_2(\theta''_{AS}=\pi)$ to sharpest peak $R_2(\theta''_{AS}=0)$) results from the switch of three cascade dressing $|G_{p1}^{T1}|^2/(\Gamma_{10}+i\Delta_{p1}^{e})+|G_1|^2+|G_2|^2$ of $\rho''^{(3)}_{AS2}$. Similar to Fig. 5(c), the broad dip (Fig. 7(f)) comes from strong destructive cross-interaction $N_2(\theta''_{AS}=\pi)$ with more phonon dressing.

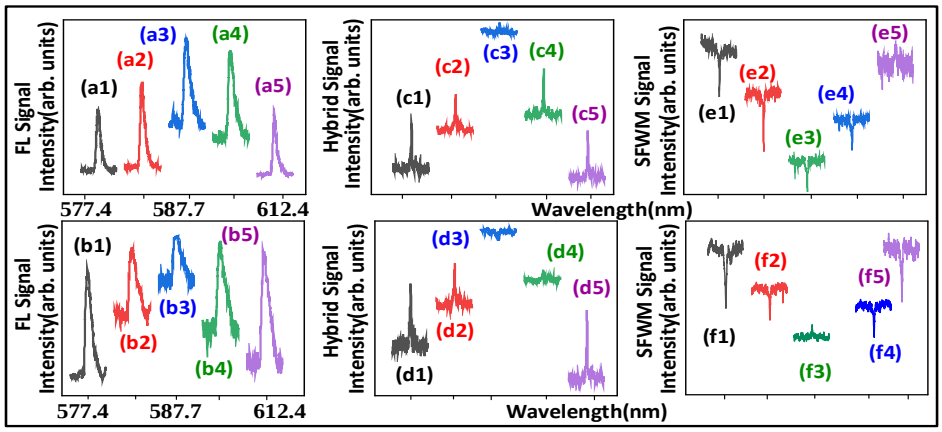

Fig. 7 (a, b) show FL cross-interaction observed from Eu^{3+} doped in molar ratio (0.5:1) $BiPO_4$ at different E_1 wavelengths (577.4nm, 584.4nm, 587.7nm, 592.4nm, 612.4nm) and E_2 scanned from 567.4nm to 607.4nm at PMT1 and PMT2, respectively, at the near time gate (1μs). Figures 7(c-d) show hybrid cross-interaction at the middle time gates (100μs). Figures 7(e-f) show SFWM cross-interaction at the far time gate (500μs). The other experimental condition is the same as Figs. 7(a, b), respectively.

Therefore, the out of phase FL constructive interaction (Figs. 7(a, b)) can be evolved to in-phase SFWM destructive interaction (Figs. 7(e, f)). The H-phase result (Figs. 5-6) comes from sensitive phonon dressing and easy distinction for in-phase SFWM.

Moreover, the linewidth of peak increases from $0.4\pm0.1nm$ in Fig. 7(c) to $4.7\pm0.1nm$ in Fig. 7(a) due to the Γ_{phonon} of generating process. The width with dressing dip increases from $0.6\pm0.1nm$ in Fig. 5(d) to $5.9\pm0.2nm$ in Fig. 3(d) due to the Γ_{phonon} of dressing process. The destructive cross-interaction R_1 in Fig. 3(d) and 5(d) results from more phonon dressing with same area. However, such more phonon dressing shows different phenomena for single sharp FL dip in Fig. 3(d) and three sharpest SFWM dips in Fig. 5(d).

3. Discussion

From our results we conclude that unlike cross-interaction N_i [non-resonance], the

 doi:10.20944/preprints202210.0389.v1

internal and external dressing atomic coherence coupling result in switching between constructive to destructive for R_i (Figs. 3(c), 4(b), 5(b, c), 7(f)). The resonant cross-interaction R_i is distinguished from non-resonant cross-interaction N_i without internal dressing.

Furthermore, the destructive interactions result from cascade dressing (Figs. 3(d, e, f), 4(c), 5(b, c), 7(e)) and four nested-cascade dressing (Fig. 5(d)), respectively. The cascade dressing and nested dressing suggest strong and stronger photon-phonon atomic coherence coupling (leading to three dressing dips shown in Fig. 5(d)), respectively.

4. Conclusion

In summary, we theoretically and experimentally studied constructive and destructive photon-phonon atomic coherence interaction. The destructive spectral interactions result from cascade dressing and four nested-cascade dressing, respectively. The cascade dressing with strong photon-phonon atomic coherence coupling lead to the single sharp dip. Moreover, the four nested-cascade dressing with stronger photon-phonon atomic coherence coupling lead to three sharp dips. The transistor as an amplifier and switch were realized by photon-phonon atomic coherence interaction, which could have potential applications in atomic-like systems.

Author Contributions: Conceptualization, Y.Z.; methodology, H.F., P.L. and Y.Z.; software, H.F.; validation, H.F., F.R. and Y.Z.; formal analysis, H.F., I.A. and Y.Z.; investigation, M.I., and F.N.; experiment, H.F., M.I. and F.N; resources, Y.Z.; data curation, H.F.; writing—original draft preparation, H.F.; writing—review and editing, H.F. and F.R.; visualization, C.L.; supervision, C.L. and P.L.; project administration, Y.Z.; funding acquisition, Y.Z. All authors have read and agreed to the published version of the manuscript.

Funding: This work was supported by the National Key Research and Development Program of China (2017YFA0303700, 2018YFA0307500), Key Scientific and Technological Innovation Team of Shaanxi Province (2021TD-56), National Natural Science Foundation of China (61975159, 11904279, 12174302, 62022066, 12074306, 12074303).

Data Availability Statement: Data underlying the results presented in this paper are not publicly available at this time but may be obtained from the authors upon reasonable request.

Conflicts of Interest: The authors declare no conflict of interest.

References

1. Lukin, M.; Yelin, S.; Fleischhauer, M.; Scully, M., Quantum interference effects induced by interacting dark resonances. Phys. Rev. A. **1999**, 60, 3225.
2. Rabl, P.; Cappellaro, P.; Gurudev Dutt, M.; Jiang, L.; Maze, J.; D. Lukin, M., Strong magnetic coupling between an electronic spin qubit and a mechanical resonator. Phys. Rev. B. **2009**, 79, 041302(R).
3. Li, P.; Xiang, Z.; Rabl, P., Nori, F., Hybrid Quantum Device with Nitrogen-Vacancy Centers in Diamond Coupled to Carbon Nanotubes. Phys. Rev. Lett. **2016**, 117, 015502.
4. Li P.; Nori, F., Hybrid Quantum System with Nitrogen-Vacancy Centers in Diamond Coupled to Surface-Phonon Polaritons in Piezomagnetic Super-lattices. Phy. Rev. A. **2018**, 10, 024011.
5. Singh, B.; Vogl, M.; Wurmehl, S.; Aswartham, S.; Büchner, B.; Kumar, P., coupling of lattice, spin, and intraconfigurational excitations of Eu^{3+} in Eu2ZnIrO6. Phys. Rev. Research. **2020**, 2. 043179.
6. Mittal, R.; Gupta, M.; Singh, B.; Pintschovius, L.; Zavartsev, Y.; Chaplot, S., Phonon dispersion relation, high-pressure phase stability, and thermal expansion in YVO_4. Phys. Rev. Materials. **2019**, 3, 043608.

7. Mishra, S.; Gupta, M.; Ningthoujam, R.; Singh, B.; Mittal, R.; Vatsa, R.; Zbiri, M.; Sharma, K.; Hansen, T.; Schober, H.; Chaplot, S., Presence of water at elevated temperatures, structural transition, and thermal expansion behavior in $LaPO_4$: Eu. Phys. Rev. Materials. **2018**, 2, 126003.
8. Li, J.; Zhu, J.; Imran, M.; Fan, H. Mujahid, A.; Nadeem, F.; Li, P.; Zhang. Y., Superior atomic coherence time controlled by crystal phase transition and optical dressing. Opt. Lett. **2022**, 47, 2310-2313.
9. Zhao, Y.; Imran, M.; Mujahid, A.; Ahmed, I.; Li, C.; Nadeem, F.; Zhang, Y., Temporal interaction of hybrid signals in various phases of Eu3+: BiPO4 through photon-phonon dressing. New J. Phys. **2022**, 24(8), 083037.
10. Passler, N.; Ni, X.; Hu, G.; Matson, J.; Carini, G.; Wolf, M.; Schubert, M.; Alù, A.; Caldwell, J.; Folland T.; Paarmann, A., Hyperbolic shear polaritons in low-symmetry crystals. Nature. **2022**, 602, 595-600.
11. Zheng, B.; Fan, J.; Chen, B.; Qin, X.; Wang, J.; Wang, F.; Deng, R.; Liu, X., Rare-Earth Doping in Nanostructured Inorganic Materials. Chem. Rev. **2022**, 122, 5519-5603.
12. Kim, J.; Chacón, R.; Wang, Z.; Larquet, E.; Lahlil, K.; Leray, A.; Colas-des-Francs, G.; Kim J.; Gacoin, T., Measuring 3D orientation of nanocrystals via polarized luminescence of rare-earth dopants. Nat. Commun. **2021**, 12, 1943.
13. Carneiro, A.; Malta, O., Glowing nanocrystals enable 3D X-ray imaging, nature. **2021**, 590, 396-397.
14. Popova, M.; Klimin, S.; Moiseev, S.; Gerasimov, K.; Minnegaliev, M.; Baibekov, E.; Shakurov, G.; Bettinelli, M.; Chou, M., Crystal field and hyperfine structure of 167Er3+ in YPO4: Er single crystals: High-resolution optical and EPR spectroscopy. Phy. Rev. B. **2019**, 99, 235151.
15. Li, P.; Li, F.; Zhang, X.; Li, Y.; Luo, X.; Wang, R.; Cai, Y.; Zhang, Y., Orthogonally polarized luminescence of single bismuth phosphate nanocrystal doped with europium. Adv. Opt. Matter. **2020**, 8(17), 2000583.
16. Li, P.; Guo, Y.; Liu, A.; Yue, X.; Yuan, T.; Zhu, J.; Zhang, Y.; Li, F., Deterministic relation between optical polarization and lattice symmetry revealed in ion-doped single microcrystals. ACS Nano. **2022**, 16(6), 9535-9545.
17. Liu, Y.; Tu, D.; Zhu H.; Chen, X., Lanthanide-doped luminescent nanoprobes: controlled synthesis, optical spectroscopy, and bioapplications. Chem. Soc. Rev. **2013**, 42, 6924–6958.
18. Serrano, D.; Kuppusamy, S.; Olaf Fuhr, B.; Hunger, D.; Ruben, M.; Goldner, P., Ultra-narrow optical linewidths in rare-earth molecular crystals. Nature. **2022**, 603, 241-246.
19. Zhong, T.; Kindem, J.; Bartholomew, J.; Rochman, J.; Craiciu, I.; Miyazono, E.; Bettinelli, M.; Cavalli, E.; Verma, V.; Nam, S.; Marsili, F.; Shaw, M.; Beyer, A.; Faraon, A.; Nanophotonic Rare-earth Quantum Memory with Optically Controlled Retrieval. Sccience. **2017**, 357, 1392-1395.
20. Ma, Y.; Ma, Y.; Zhou, Z.; Li, C.; Guo, G., Onehour Coherent Optical Storage in an Atomic Frequency Comb Memory. Nat. Commun. **2021**, 12, 2381.
21. Zhang, Y.; Khadka, U.; Anderson, B.; Xiao, M., Temporal and Spatial Interference between Four-Wave Mixing and Six-Wave Mixing Channels. Phys. Rev. Lett. **2009**, 102, 013601.
22. Li, P.; Zheng, H.; Zhang, Y.; Sun, J.; Li, C.; Huang, G.; Zhang, Z.; Y. Li, Y.; Zhang, Y., Controlling the transition of bright and dark states via scanning dressing field. Opt. Materials. **2013**, 35, 1062–1070.
23. Nie, Z.; Zheng, H.; Li, P.; Yang, Y.; Zhang, Y.; Xiao, M., Interacting multi-wave mixing in a five-level folding atomic system. Phys. Rev. A. **2008**, 77, 063829.
24. Fan, H.; Raza, F.; Ahmed, I.; Li, K. Ullah, H.; Zhang, Y., Three-type Fano interference controlled by the phase transition of Eu^{3+}/ Pr^{3+}: YPO_4. New J. Phys. **2020**, 22, 093008.
25. Li, B.; Jiang, Z.; Zhang, Y.; Zhang, Z.; Wen, F.; Chen, H.; Zhang Y.; Xiao M., Controlled Correlation and Squeezing in Pr^{3+}: Y_2SiO_5 to Yield Correlated Light Beams. Phys. Rev. Applied. **2017**, 7, 014023.